ChemComm

ROYAL SOCIETY OF CHEMISTRY

COMMUNICATION

View Article Online
View Journal | View Issue

Check for updates

Cite this: *Chem. Commun.*, 2026, **62**, 9254

Received 6th April 2026,
Accepted 17th April 2026

DOI: 10.1039/d6cc02096h

rsc.li/chemcomm

Stabilizing CuTCNQ cathodes in sulfide-based all-solid-state organic lithium batteries *via* a fluoroiodinated molecular modifier

Wenwen Deng,*[ab] Ying Zhou,[c] Yuanyuan Quan,[c] Yuhang Guo,[a] Tianxiang Wei[a] and Zhong Jin *[b]

A fluoroiodinated molecular modifier, $C_6F_{13}I$, is introduced to stabilize the CuTCNQ/Li_6PS_5Cl interface in sulfide-based all-solid-state organic lithium batteries. Its electrochemical activation generates a conformal LiF/LiI/organofluorinated interphase, suppressing electrolyte decomposition, preserving Li^+ transport, and markedly improving the rate capability and cycling stability of the CuTCNQ cathode.

Organic electrode materials (OEMs) have emerged as promising candidates for next-generation rechargeable batteries because of their structural diversity, molecular tunability, sustainability, and compatibility with scalable green manufacturing.[1–4] When coupled with nonflammable solid-state electrolytes (SSEs), they enable all-solid-state lithium-organic batteries (ASSOLBs), which combine intrinsic safety with the versatile redox chemistry of organic materials.[5,6] Among the available SSEs, sulfide electrolytes are particularly attractive owing to their high room-temperature ionic conductivity, low interfacial resistance, and quasi-glassy deformability, which enables intimate solid–solid contact under relatively low stack pressure.[7]

However, the practical development of sulfide-based ASSOLBs remains severely hindered by cathode-side interfacial instability. The limited oxidative stability of sulfide electrolytes leads to anodic decomposition during charging, especially at elevated potentials, generating resistive interphases that impede Li^+ transport, increase charge-transfer resistance, and accelerate capacity decay.[8] Stabilizing the cathode/electrolyte interface is therefore essential for high-performance sulfide-based ASSOLBs.

In this context, CuTCNQ, a semiconducting metal–organic charge-transfer compound constructed from Cu^+ and the strongly electron-accepting TCNQ ligand, represents an appealing cathode platform.[9] Owing to its favorable electronic conductivity, particularly in phase-I,[10] CuTCNQ is well suited for probing the role of cathode-side interfacial regulation in sulfide-based ASSOLBs. Nevertheless, under high-voltage operation, direct contact with sulfide electrolytes is expected to induce parasitic interfacial reactions, thereby compromising Li^+ transfer and cycling reversibility. Although microstructural strategies such as freeze grinding and solvent-assisted coating have been explored to mitigate such degradation,[11,12] molecularly defined regulation of organic cathode/sulfide electrolyte interfaces remains largely unexplored. Here, we introduce $C_6F_{13}I$ as a molecular interfacial modifier for CuTCNQ-based sulfide ASSOLBs. Its weak C–I bond and fluorinated structure enable the formation of a robust LiF/LiI-rich interphase at the CuTCNQ/LPSC interface, which suppresses parasitic interfacial reactions while preserving efficient Li^+ transport. As a result, the modified CuTCNQ-4 cathode delivers improved reversible capacity, rate capability, and cycling stability, retaining 60% of its capacity after 100 cycles at 0.5 C. Combined TEM, XPS, and operando pressure-monitoring results further reveal that this molecular strategy effectively regulates both the interfacial chemistry and the mechanical evolution of the CuTCNQ cathode, providing a viable route toward high-performance sulfide-based ASSOLBs.

CuTCNQ was synthesized through a rapid coordination reaction between CuI and TCNQ in acetonitrile under an argon atmosphere, as schematically illustrated in Fig. 1a.[13] Upon brief stirring, Cu^+ coordinates with the cyano groups of TCNQ to form an extended coordination network, yielding phase-I CuTCNQ. The crystal structure (Fig. 1b) consists of alternating Cu centres and TCNQ units, forming rod-like crystalline motifs with well-defined orientations. SEM images (Fig. S1a) show that the as-prepared CuTCNQ displays a rod-like morphology with

---

[a] *School of Materials Science and Engineering, Anhui University, 230601 Hefei, Anhui, PR China. E-mail: 24177@ahu.edu.cn*

[b] *State Key Laboratory of Coordination Chemistry, MOE Key Laboratory of Mesoscopic Chemistry, MOE Key Laboratory of High Performance Polymer Materials and Technology, Jiangsu Key Laboratory of Clean Energy Catalysis and Intelligent Green Chemical Engineering, Suzhou Key Laboratory of Green Intelligent Manufacturing of New Energy Materials and Devices, Tianchang New Materials and Energy Technologies Research Center, Institute of Green Chemistry and Engineering, School of Chemistry and Chemical Engineering, Nanjing University, Nanjing, Jiangsu, 210023, China. E-mail: zhongjin@nju.edu.cn*

[c] *School of Material Science and Engineering, Suzhou University of Science and Technology, Suzhou, 215000, China*

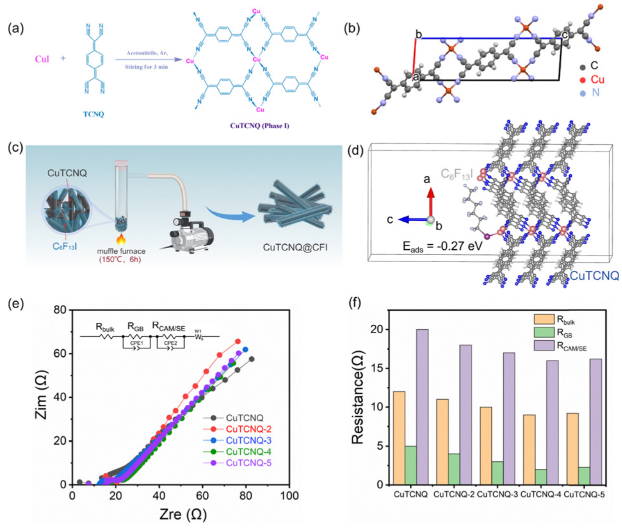

Fig. 1 (a) Schematic illustration of the synthesis of CuTCNQ (phase-I); (b) crystal structure of CuTCNQ (phase I); (c) schematic of illustration of the synthesis of CuTCNQ-CFI composite; (d) DFT-optimized adsorption configuration of a $C_6F_{13}I$ fragment on the CuTCNQ surface; (e) Nyquist plots of CuTCNQ and CuTCNQ-CFIx symmetric cells at room temperature with the equivalent circuit model shown in the inset; (f) corresponding fitted resistance values of R_{bulk}, R_{GB}, and $R_{CAM/SE}$.

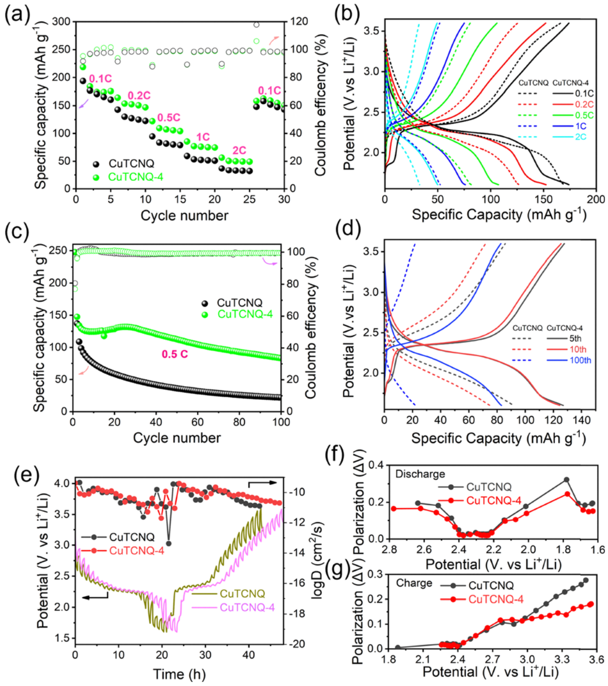

Fig. 2 (a) Rate capability at 60 °C tested under 0.1, 0.2, 0.5, 1, and 2 C; (b) corresponding charge–discharge profiles of CuTCNQ and CuTCNQ-4 at different C-rates (0.1–2 C); (c) long-term cycling performance at 0.5 C and 60 °C; (d) charge–discharge voltage profiles of CuTCNQ and CuTCNQ-4 during the 5th, 50th, and 100th cycles at 0.5 C; (e) GITT profiles obtained by applying a series of current pulses followed by 30 min relaxation for each step; Voltage polarization (Δ*V*) plots during (f) discharge and (g) charge processes.

widths below 1 μm and lengths of approximately 10–20 μm. To introduce molecular-level interfacial regulation, CuTCNQ crystals were treated with $C_6F_{13}I$ *via* thermal adsorption (Fig. 1c). Heating at 150 °C for 6 h in a sealed environment enables interfacial adsorption and anchoring of $C_6F_{13}I$ on the CuTCNQ surface. DFT calculations further reveal a negative adsorption energy (E_{ads} = −0.27 eV) for $C_6F_{13}I$ on the CuTCNQ (020) plane (Fig. 1d), indicating thermodynamically favourable interfacial binding.

Fig. S1b–f show that introducing different amounts of $C_6F_{13}I$ do not noticeably alter the morphology of CuTCNQ. The XRD patterns (Fig. S2a) can all be indexed to phase-I CuTCNQ, consistent with the reported structure,[13] and no new peaks or obvious peak shifts are observed after modification, indicating preserved structural integrity. FT-IR spectra (Fig. S2b) further confirm the CuTCNQ framework, showing characteristic bands at 2196, 2165, 1573, 1507, 1325, 1175, 988, and 823 cm^{-1}. The band at 2196 cm^{-1} is assigned to C≡N stretching, while the absorption at 823 cm^{-1} is characteristic of $TCNQ^-$, excluding the presence of neutral TCNQ or $TCNQ^{2-}$.[14]

The electrochemical effect of surface modification was first evaluated by EIS using five CuTCNQ-*x* cathodes (Fig. 1e), where *x* represents the amount of $C_6F_{13}I$ (ul) used for the surface modification. The impedance mainly comprises the bulk resistance (R_{bulk}), grain-boundary resistance (R_{GB}), and interfacial resistance ($R_{CAM/SE}$).[15] As summarized in Fig. 1f, all samples exhibit similar R_{bulk} values of 8–12 Ω, corresponding to the intrinsic resistance of the solid electrolyte, while R_{GB} remains below 5 Ω with only minor variation. In contrast, $R_{CAM/SE}$ differs markedly among the samples: pristine CuTCNQ shows the highest value (22.98 Ω), which progressively decreases upon $C_6F_{13}I$ introduction and reaches a minimum of 12.49 Ω for CuTCNQ-4. No further appreciable decrease is observed for CuTCNQ-5, suggesting that interfacial optimization becomes saturated at the CuTCNQ-4 composition. CuTCNQ-4 was therefore selected for subsequent study.

Fig. 2a compares the rate performance of Li/LPSC/CuTCNQ and Li/LPSC/CuTCNQ-4 batteries (60 °C). The Li/LPSC/CuTCNQ-4 battery (mass loading: 1.6 mg cm^{-2}) delivers discharge capacities of 184.2, 153.7, 109.5, 77.0, and 50.7 mAh g^{-1} at 0.1, 0.2, 0.5, 1, and 2 C, respectively, whereas the corresponding values for Li/LPSC/CuTCNQ are 176.9, 130.2, 83.5, 53.5, and 33.5 mAh g^{-1}. Although both electrodes show comparable capacities at 0.1 C, CuTCNQ-4 consistently outperforms CuTCNQ at higher rates. As shown in Fig. 2b, Li/LPSC/CuTCNQ-4 also exhibits smaller polarization and better-defined voltage plateaus, indicative of faster ion/electron transport kinetics. Long-term cycling at 0.5 C (Fig. 2c) further demonstrates the superior durability of Li/LPSC/CuTCNQ-4, which retains a reversible capacity of ∼140 mAh g^{-1} with 60% capacity retention after 100 cycles. By contrast, Li/LPSC/CuTCNQ rapidly decays to ∼60 mAh g^{-1} (25% retention). The corresponding charge/discharge profiles (Fig. 2d) show that CuTCNQ-4 maintains stable voltage plateaus and higher capacities upon cycling, whereas pristine CuTCNQ undergoes pronounced polarization growth and capacity fading. Similar trends are preserved at higher mass loadings (2.4 and 3.2 mg cm^{-2}) (Fig. S3), where CuTCNQ-4 still delivers higher capacity and better cycling stability. These results indicate that the formed LiF/LiI interphase effectively stabilizes the CuTCNQ/LPSC interface, leading to improved Li^+ reversibility, reduced polarization, and enhanced rate and cycling performance.

Consistent with the CV response, *b*-value analysis, and capacitive contribution in Fig. S4, interfacial modification promotes pseudocapacitive-dominated charge storage and accelerates electrochemical kinetics. The performance enhancement was further probed by GITT and operando pressure monitoring. As shown in Fig. 2e, Li/LPSC/CuTCNQ-4 exhibits a slightly higher Li^+ diffusion coefficient than Li/LPSC/CuTCNQ during discharge and, more importantly, retains distinctly higher diffusion coefficients near the charge cutoff, indicating more efficient Li^+ transport under kinetically demanding high-voltage conditions. This trend is also reflected in the voltage polarization (ΔV, Fig. 2f and g). During discharge, CuTCNQ-4 shows slightly lower polarization at the initial lithiation stage and consistently smaller ΔV at lower voltages, indicating reduced interfacial resistance buildup during deep lithiation. During charging, CuTCNQ-4 likewise maintains lower ΔV throughout the process, particularly in the 3.0–3.6 V region and near the charge cutoff, highlighting its improved resistance to high-voltage interfacial deterioration. These results, in concert with the GITT analysis, confirm that the formed LiF/LiI interphase promotes Li^+ transport and enables a more stable cathode/electrolyte interface.

Operando stress monitoring further reveals the mechanical effect of the formed LiF/LiI interphase (Fig. S5). Because both cells use the same electrolyte and lithium anode, the stress evolution mainly reflects cathode-side volume changes and side reactions. In both cases, stress decreases during discharge and increases during charge, consistent with reversible electrode breathing. However, while Li/LPSC/CuTCNQ exhibits a gradual decay in overall pressure during cycling, Li/LPSC/CuTCNQ-4 shows much more reversible stress fluctuations. Although both cells display similar stress changes during the first discharge, the pristine CuTCNQ cell shows incomplete stress recovery upon charging, indicative of persistent parasitic interfacial reactions. In contrast, the formed LiF/LiI interphase suppresses these side reactions and enables more reversible Li^+ migration, resulting in mechanically more stable cycling. This agrees well with the improved capacity retention of Li/LPSC/CuTCNQ-4 and further underscores the role of the CFI-derived interphase in stabilizing both the electrochemical and mechanical evolution of the solid-state cell.

The mechanism underlying the $C_6F_{13}I$-induced enhancement in the electrochemical performance of the CuTCNQ battery was investigated by thermogravimetric analysis (TGA), transmission electron microscopy (TEM), and X-ray photoelectron spectroscopy (XPS) on the pristine CuTCNQ and CuTCNQ-4 composite cathodes. As shown in Fig. S6, both samples show negligible mass loss below 300 °C, while CuTCNQ-4 exhibits a broader mass-loss profile at higher temperatures, indicating altered thermal decomposition behavior. To gain deep insight into the origin of this altered thermal behavior, the morphology and surface structure of the cathodes were further examined by TEM. As shown in Fig. 3a, pristine CuTCNQ exhibits a smooth surface, whereas CuTCNQ-4 is covered by a conformal layer with a thickness of 20 nm (Fig. 3b and c). Corresponding energy-dispersive X-ray spectroscopy (EDS) elemental mapping (Fig. 3d–i) reveals a homogeneous distribution of the constituent elements, including fluorine and iodine, confirming the uniform coverage of the fluorinated iodine-containing layer.

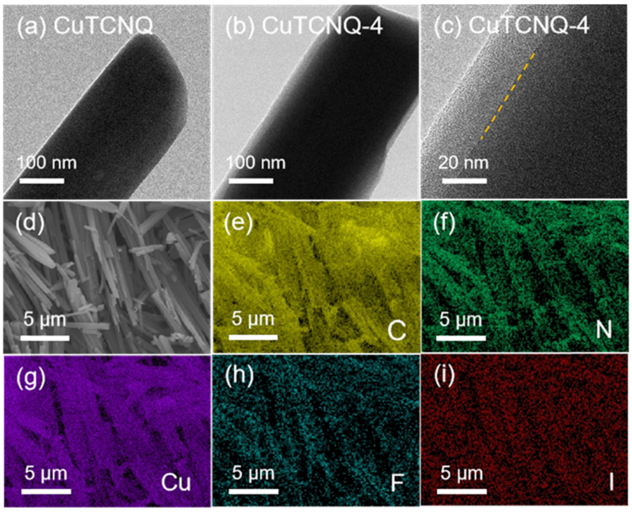

Fig. 3 (a)–(c) TEM images of CuTCNQ and CuTCNQ-4; (d–i) EDS elemental mapping of CuTCNQ-4.

While TEM and EDS mapping confirm the presence and uniform coverage of the fluorinated iodine-containing surface layer, XPS was further employed to clarify its chemical composition and interfacial evolution after contact with LPSC. As shown in Fig. 4a and b, a characteristic C–F signal at 688.8 eV (blue-shaded region), originating exclusively from the $C_6F_{13}I$ additive, is clearly observed both before and after mixing CuTCNQ-4 with LPSC. After mixing Li_6PS_5Cl, a new feature appears at 684.9 eV, corresponding to Li–F bonding, evidencing the interfacial formation of LiF. The I 3d XPS spectrum in Fig. S7 shows characteristic I $3d_{5/2}$ and I $3d_{3/2}$ peaks at 619.6 and 631.1 eV, respectively, indicative of interfacial LiI formation. The formation mechanism can be rationalized in Scheme S1. Specifically, owing to the intrinsically low bond dissociation

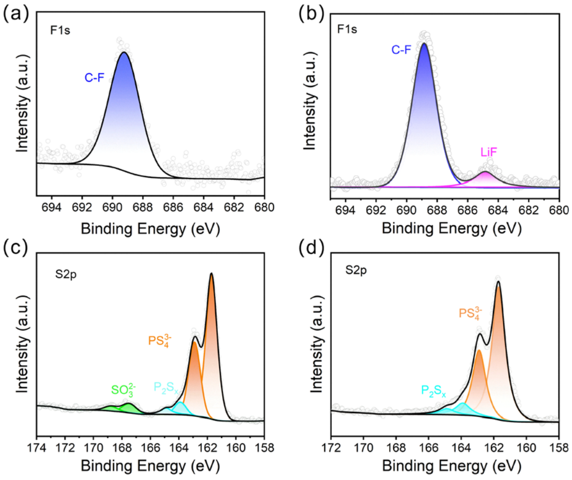

Fig. 4 F 1s spectra of (a) CuTCNQ-4 and (b) CuTCNQ-4/LPSC composite. S 2p spectra of (c) CuTCNQ/LPSC and (d) CuTCNQ-4/LPSC composite.

energy of the C–I bond and the strong electron-withdrawing nature of the perfluoroalkyl chain, $C_6F_{13}I$ readily undergoes C–I bond cleavage upon contact with LPSC. Subsequent interaction with LPSC allows abundant Li^+ species in the electrolyte to react with the fluorinated fragments, thereby triggering defluorination reactions and preferential formation of LiF. Moreover, the LiF/LiI-derived interphase plays a critical role in stabilizing the LPSC interface. As shown in Fig. 4c and d, both composite electrodes exhibit the characteristic PS_4^{3-} peak at 161.7 eV from LPSC, along with a P_2S_x signal at 163.9 eV. Notably, the CuTCNQ/LPSC sample shows an additional weak SO_3^{2-} peak at 166.8 eV, indicative of slight interfacial oxidation, possibly caused by residual oxygen-containing species from synthesis or unavoidable air exposure during sample transfer. In contrast, the SO_3^{2-} signal is absent in the CuTCNQ-4/LPSC composite, further confirming that the LiF/LiI-derived interphase effectively improves the interfacial chemical stability of the sulfide electrolyte.

In summary, a fluoroiodinated molecular modifier, $C_6F_{13}I$, is introduced to stabilize the CuTCNQ/LPSC interface in sulfide-based all-solid-state organic lithium batteries. The $C_6F_{13}I$ treatment forms a conformal surface layer on CuTCNQ and further enables the *in situ* generation of a LiF/LiI-rich interphase upon contact with the sulfide electrolyte, thereby suppressing interfacial side reactions while preserving efficient Li^+ transport. Consequently, the modified CuTCNQ-4 cathode exhibits lower cathode/electrolyte interfacial resistance, improved rate capability, and markedly enhanced cycling stability relative to pristine CuTCNQ. Combined TEM, XPS, GITT, voltage-polarization, and operando stress analyses further show that the CFI-derived interphase effectively mitigates high-voltage interfacial deterioration and promotes more reversible electrochemical and mechanical evolution during cycling. This work provides a simple molecular strategy for stabilizing organic cathode/sulfide electrolyte interfaces in high-performance ASSOLBs.

Conflicts of interest

There are no conflicts to declare.

Data availability

The authors confirm that the data supporting the findings of this study are available within the article and its supplementary information (SI). Supplementary information: detailed experimental procedures, materials synthesis, characterization data, electrochemical measurements, and additional figures and scheme. See DOI: https://doi.org/10.1039/d6cc02096h.

Acknowledgements

This work was funded by The Natural Science Foundation of the Jiangsu Higher Education Institutions of China (23KJB150032, 24KJA15004), the National Natural Science Foundation of China (U25A20628, 22561160129, 22479074, 22475096), the Equipment Pre-Research and Ministry of Education Joint Fund (8091B02052407), the Fundamental Research Program Key Project of Jiangsu Province (BK20253008), the Science and Technology Major Project of Jiangsu Province (BG2024013), the Scientific and Technological Achievements Transformation Special Fund of Jiangsu Province (BA2023037), the Academic Degree and Postgraduate Education Reforming Project of Jiangsu Province (JGKT24_C001), the Key Core Technology Open Competition Project of Suzhou City (SYG2024122), the Open Research Fund of Suzhou Laboratory (SZLAB-1308-2024-TS005), the Chenzhou National Sustainable Development Agenda Innovation Demonstration Zone Provincial Special Project (2023sfq11), and the Fundamental Research Funds for the Central Universities and Nanjing University International Collaboration Initiative (020514380354). The authors would like to thank Nan Wu from Shiyanjia Lab (www.shiyanjia.com) for the XPS analysis.

References

1 Y. Lu and J. Chen, *Nat. Rev. Chem.*, 2020, **4**, 127–142.
2 W. Deng, N. Zhang, Y. Zhou, Y. Quan, L. Yao, C. Zhang, Y. Huang and Z. Jin, *Chem. Commun.*, 2026, **62**, 4601–4604.
3 W. Deng, W. Shi, P. Li, N. Hu, S. Wang, J. Wang, L. Liu, Z. Shi, J. Lin and C. Guo, *Energy Storage Mater.*, 2022, **46**, 535–541.
4 Y. Quan, W. Deng, Q. Ma, C. Guo and Z. Jin, *Nano Lett.*, 2026, **26**, 1019–1026.
5 L. Zhao, A. E. Lakraychi, Z. Chen, Y. Liang and Y. Yao, *ACS Energy Lett.*, 2021, **6**, 3287–3306.
6 W. Deng, Y. Zhou, X. Feng, Q. Ma, L. Li, Y. Guo, W. Huang, L. Zhu, L. Deng and Y. Wang, *Angew. Chem., Int. Ed.*, 2026, **65**, e24363.
7 Q. Zhang, D. Cao, Y. Ma, A. Natan, P. Aurora and H. Zhu, *Adv. Mater.*, 2019, **31**, 1901131.
8 Y. Tian, T. Shi, W. D. Richards, J. Li, J. C. Kim, S.-H. Bo and G. Ceder, *Energy Environ. Sci.*, 2017, **10**, 1150–1166.
9 C. Fang, Y. Huang, L. Yuan, Y. Liu, W. Chen, Y. Huang, K. Chen, J. Han, Q. Liu and Y. Huang, *Angew. Chem.*, 2017, **129**, 6897–6901.
10 R. A. Heintz, H. Zhao, X. Ouyang, G. Grandinetti, J. Cowen and K. R. Dunbar, *Inorg. Chem.*, 1999, **38**, 144–156.
11 F. Hao, Y. Liang, Y. Zhang, Z. Chen, J. Zhang, Q. Ai, H. Guo, Z. Fan, J. Lou and Y. Yao, *ACS Energy Lett.*, 2021, **6**, 201–207.
12 J. Zhang, Z. Chen, Q. Ai, T. Terlier, F. Hao, Y. Liang, H. Guo, J. Lou and Y. Yao, *Joule*, 2021, **5**, 1845–1859.
13 C. A. Fernandez, P. C. Martin, T. Schaef, M. E. Bowden, P. K. Thallapally, L. Dang, W. Xu, X. Chen and B. P. McGrail, *Sci. Rep.*, 2014, **4**, 6114.
14 Z. Hussain, A. Nafady, S. R. Anderson, A. M. Al-Enizi, A. A. Alothman, R. Ramanathan and V. Bansal, *Nanomaterials*, 2021, **11**, 954.
15 P. Vadhva, J. Hu, M. J. Johnson, R. Stocker, M. Braglia, D. J. L. Brett and A. J. E. Rettie, *ChemElectroChem*, 2021, **8**, 1930–1947.